

30. K. M. O'Hara, S. L. Hemmer, M. E. Gehm, S. R. Granade, J. E. Thomas, *Science* **298**, 2179–2182 (2002).
 31. C. Fort *et al.*, *Phys. Rev. Lett.* **95**, 170410 (2005).
 32. L. Sanchez-Palencia *et al.*, *Phys. Rev. Lett.* **98**, 210401 (2007).
 33. M. Greiner, O. Mandel, T. Esslinger, T. W. Hänsch, I. Bloch, *Nature* **415**, 39–44 (2002).
 34. Y. Castin, *C. R. Phys.* **5**, 407–410 (2004).
 35. L. P. Pitaevskii, A. Rosch, *Phys. Rev. A* **55**, R853–R856 (1997).
 36. E. Vogt *et al.*, *Phys. Rev. Lett.* **108**, 070404 (2012).
 37. J. Hofmann, *Phys. Rev. Lett.* **108**, 185303 (2012).
 38. E. Taylor, M. Randeria, *Phys. Rev. Lett.* **109**, 135301 (2012).
 39. C. Gao, Z. Yu, *Phys. Rev. A* **86**, 043609 (2012).

40. Y. Nishida, S. Moroz, D. T. Son, *Phys. Rev. Lett.* **110**, 235301 (2013).
 41. A. G. Volosniev, D. V. Fedorov, A. S. Jensen, N. T. Zinner, *J. Phys. At. Mol. Opt. Phys.* **47**, 185302 (2014).
 42. C. Gao, J. Wang, Z. Yu, *Phys. Rev. A* **92**, 020504 (2015).

ACKNOWLEDGMENTS

We thank P. Zhang for helpful discussions. This research is supported by the National Natural Science Foundation of China (NSFC) (grant nos. 11374101 and 91536112) and the Shu Guang project (14SG22) of Shanghai Municipal Education Commission and Shanghai Education Development Foundation. Z.S. and H.Z. are supported by MOST (grant no. 2016YFA0301604), Tsinghua University Initiative Scientific Research Program and

NSFC grant no. 11325418. R.Q. is supported by the Fundamental Research Funds for the Central Universities and the Research Funds of Renmin University of China under grant no. 15XNL18 and no. 16XNLQ03.

SUPPLEMENTARY MATERIALS

www.sciencemag.org/content/353/6297/371/suppl/DC1
 Materials and Methods
 Supplementary Text
 Figs. S1 to S3
 Table S1
 References (43, 44)

13 December 2015; accepted 21 June 2016
 10.1126/science.aaf0666

PHYSICS

Electron microscopy of electromagnetic waveforms

A. Ryabov^{1,2} and P. Baum^{1,2*}

Rapidly changing electromagnetic fields are the basis of almost any photonic or electronic device operation. We report how electron microscopy can measure collective carrier motion and fields with subcycle and subwavelength resolution. A collimated beam of femtosecond electron pulses passes through a metamaterial resonator that is previously excited with a single-cycle electromagnetic pulse. If the probing electrons are shorter in duration than half a field cycle, then time-frozen Lorentz forces distort the images quasi-classically and with subcycle time resolution. A pump-probe sequence reveals in a movie the sample's oscillating electromagnetic field vectors with time, phase, amplitude, and polarization information. This waveform electron microscopy can be used to visualize electrodynamic phenomena in devices as small and fast as available.

Electron microscopy works at wavelengths 100,000× smaller than that of light and therefore allows studying matter and materials with subatomic resolution (1, 2). With added temporal resolution, ultrafast reaction paths in physical and chemical transitions can also be recorded (3, 4).

Rather elusive for electron microscopy, however, have been electrodynamic phenomena, although oscillating currents and fields are fundamental to the operation of almost any information processing device or metamaterial. Based on differential phase contrast (5, 6), ptychography (7), or laser-electron energy exchange techniques (8), electron microscopy studies on electromagnetism could reveal electrostatic field distributions (9–11), ultrafast carrier diffusions (12, 13), or cycle-averaged nanophotonic dynamics (14–16), but so far not the fundamental electromagnetic waveforms with their rapidly oscillating field vectors.

We merged the electron microscope's supremacy in matter characterizations with a subcycle and subwavelength access to electromagnetic phenomena (Fig. 1). Femtosecond electron pulses (Fig. 1, blue) at 70 keV central energy are generated by pulsed-laser photoemission (17). The electron wave-

packets (18) are further compressed in time by a terahertz field (Fig. 1, red) in grazing incidence to a foil (19). Alternatives here could be beam blanking (20), microwave compression (18), photon-gating (21), or ponderomotive bunching (22). A magnetic lens (Fig. 1, gray) widens the beam for passage through the sample with close-to-zero divergence. The proof-of-principle sample is a metal split-ring resonator (Fig. 1, yellow), which is a typical building block for metamaterials (23) or surfaces (24) with optical effects otherwise not available (25, 26). The resonator with ~250 μm radius is excited with a single-cycle, phase-locked electromagnetic pulse of 0.1 to 0.8 THz bandwidth (17). It propagates along the z axis with a linear polarization oriented ~5° off the y axis. The electron pulse duration at the sample is ~15 times shorter than the excitation half-cycle. An objective magnetic lens (Fig. 1, gray) magnifies the shadowed electron beam onto a screen (Fig. 1, green). Some intentional defocus makes the scheme sensitive to local beam deflections (Fig. 1, dotted lines) and allows concluding from the distorted screen images, taken at a sequence of electron/field delay times, to the time-frozen electrodynamics in the sample.

First results are shown in Fig. 2, obtained with the excitation field depicted in Fig. 2A and at a magnification of about 5×. The electron pulses are characterized by streaking (19) and have 80-fs duration (Fig. 2B). The resonator, which was laser-machined into 30-μm-thick aluminum foil (Fig. 2C), shows some imperfections,

in particular fringing edges and off-center circles. An isosurface of the time-dependent shadow pattern deformations reveals pronounced temporal oscillations (Fig. 2D). The raw images (shown

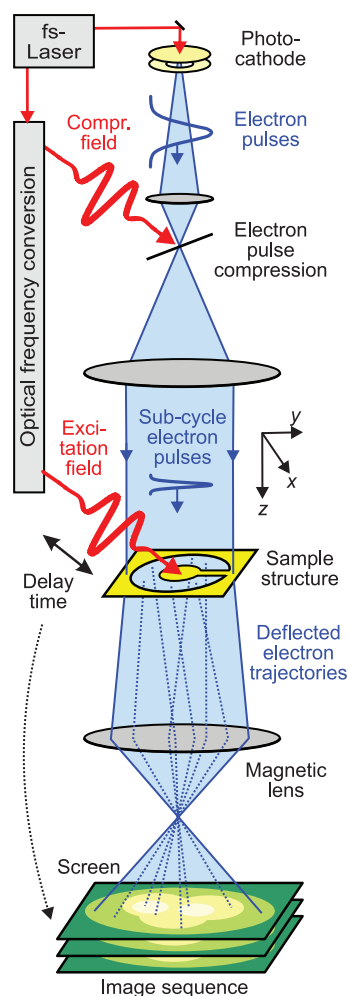


Fig. 1. Concept and experimental setup. A femtosecond laser produces single-cycle terahertz pulses (red) and a beam of femtosecond electron pulses (blue). The terahertz radiation compresses the electrons in time and also triggers electromagnetic resonance in the sample (yellow). The electron pulses are locally and instantaneously distorted (dotted lines) and therefore reveal the electrodynamics of the sample.

¹Ludwig-Maximilians-Universität München, Am Coulombwall 1, 85748 Garching, Germany. ²Max Planck Institute of Quantum Optics, Hans-Kopfermann-Strasse 1, 85748 Garching, Germany.

*Corresponding author. Email: peter.baum@lmu.de

for a subset of pump-probe delays (in Fig. 2E) become distorted in a self-overlapping way before returning to the original at later times (movie S1). Another example of raw data is shown in movie S2.

For analyzing our experiment, we denote the spatiotemporal electric and magnetic fields around the resonator with $E(x, y, z, t)$ and $B(x, y, z, t)$. $v_{el} \approx 0.53c$ is the electron velocity (c , speed of light), $\tau_{el} \approx 80$ fs (full width at half maximum) is the electron pulse duration, $f_{max} \approx 0.8$ THz is the highest frequency excited, $D_z \approx 30$ μm is the mode thickness along the z axis, and $\alpha_{em} \approx 60$ μrad (root mean square) is the beam divergence at the sample (~ 20 nm source emittance and ~ 340 μm beam radius). We make these approximations: (i) $\tau_{el} \ll 1/f_{max}$, the electron pulses are much shorter than a wave cycle; (ii) $D_z/v_e \ll 1/f_{max}$, subcycle transition time; (iii) $\alpha_{em} \approx 0$, the probe beam is collimated; (iv) two-dimensional fields $E_{x,y}(x, y, t)$ and $B_{x,y}(x, y, t)$ suitably describe the resonator response; and (v) magnetic fields are negligible (17). Conditions (i) and (ii) are essential to the concept, and (iii) to (v) are specific to the particular geometry. With m_e and e the electron mass and charge, respectively, we obtain for the change in angles $\alpha_{x,y}$ at each position in the beam, at each pump-probe delay τ

$$\alpha_{x,y}(x, y, \tau) \approx \frac{eE_{x,y}(x, y, \tau)D_z}{m_e v_e^2} \quad (1)$$

Each ray in the electron beam profile acquires a local-field-dependent momentum kick that is di-

rectly proportional to the local waveform, frozen in time at the chosen probe delay.

On the screen, electrons from faraway locations can end up at the same positions, and inversion is nonbijective. We therefore measured for each pump-probe delay a batch of screen images, in which the excitation peak field strength E_{exc} is gradually increased from zero to the available maximum. Because of the collimated illumination, this method is related to measuring the evolution of the distorted beam profile along the z axis. The data set is four-dimensional and comprises 250 by 250 image pixels, 150 pump-probe delays, and 16 different excitation field strengths. At a 50-kHz pump-probe repetition rate, the total accumulation time is ~ 1 hour. We calculated $\alpha_{x,y}(x, y, \tau)$ for each delay step with a least-square fitting algorithm (17) and $E_{x,y}(x, y, \tau)$ via Eq. 1.

Shown in Fig. 3A are three vector-field snapshots at 2.8, 3.2, and 3.8 ps delay, respectively, as a subset of the full results (movie S3). The triangle tips denote the vectorial direction, and field strength is encoded in color and size. Some high-frequency temporal noise was diminished with a low-pass Gaussian filter at 1 THz. The vector field at 2.8 ps shows three local maxima (Fig. 3A, top, right, and left). We see an asymmetry in x , a predominantly radial polarization everywhere, and at each angle, a radially decreasing field strength. The peak field is 7 V/ μm , which is ~ 3.5 times higher than the driving field. Shown in Fig. 3B are the time-dependent electric fields at two selected positions (Fig. 3A, white circles), and the time-dependent polarization is plotted in Fig. 3B, right. The fields

initially follow the single-cycle excitation pulse, but after ~ 4 ps, when the excitation has diminished, they evolve into slower oscillation cycles with decaying amplitude. Fitting each such time trace with a damped-harmonic oscillator model reveals a map of central frequencies (0.27 to 0.30 THz), dampings (3 to 6 ps), and group delays (± 0.1 ps). These ranges indicate that a single delocalized mode is predominant after the excitation.

An analysis of the collective carrier motion causing the observed near-field dynamics is shown in Fig. 3C. The surface charge density $\sigma = \epsilon_0 E_{\perp}$ is plotted along a path around the inner edge of the resonator. The peak charge is ~ 400 e/ μm^2 , and ~ 20 e/ μm^2 are detectable above the noise. Three spatial regions are evident, one at the top ($\pm 180^\circ$) and two others left and right of the gap ($\sim \pm 45^\circ$). The dynamics around the gap extend by more than $\pm 90^\circ$ and the phase is shifted with respect to the top region. Some features in Fig. 3C have a tilt, indicating in part an azimuthally traveling excitation, which is also observable in the raw data and result movies (movies S1 and S3, respectively). Circular motion ceases after ~ 4 ps, and the remaining dynamics are mostly symmetric with the x axis. It appears that the excitation first localizes at the gap and top half, while subsequently creating a spread out, rather symmetric, and longer lived mode with mostly radial polarization.

Next, we used our waveform electron microscopy to characterize a rectangular aperture and butterfly resonator, which are typical elements for field enhancement in optics. A snapshot at 2.2 ps delay of the field in the slit (730 by 100 μm^2) is shown in

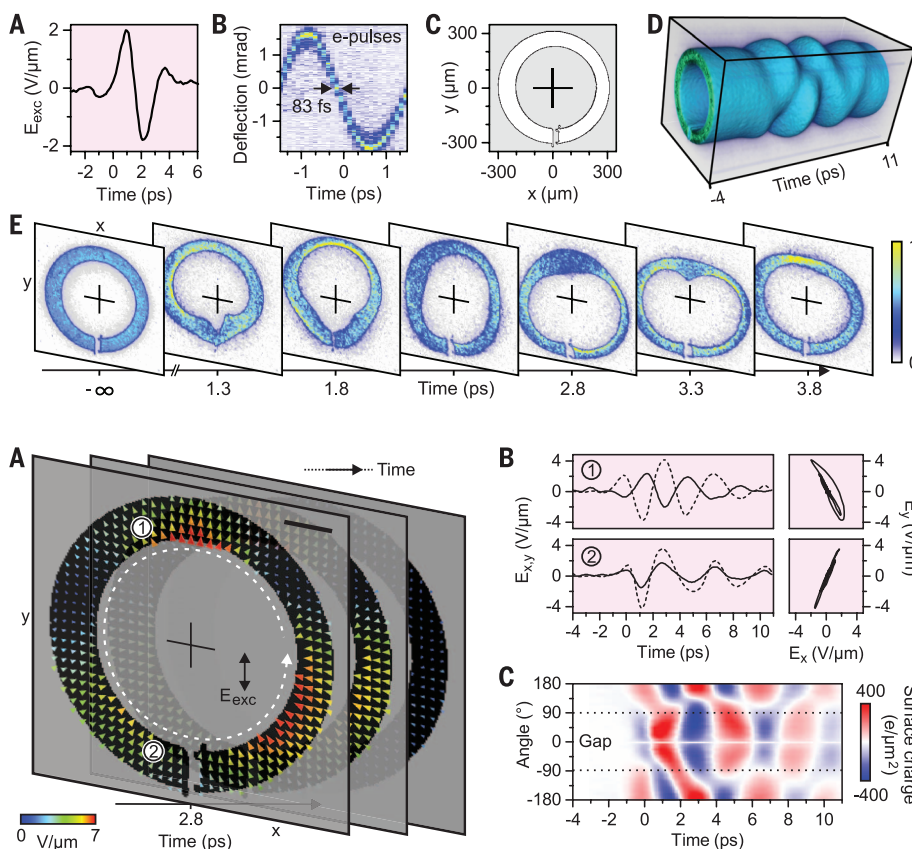


Fig. 2. Waveform microscopy results. (A) Electric field for sample excitation. (B) Electron pulse characterization (19). (C) Shape of the split-ring resonator. (D) Isosurface of the time-dependent shadow images. (E) Subset of raw images on the screen (full results in movies S1 and S2).

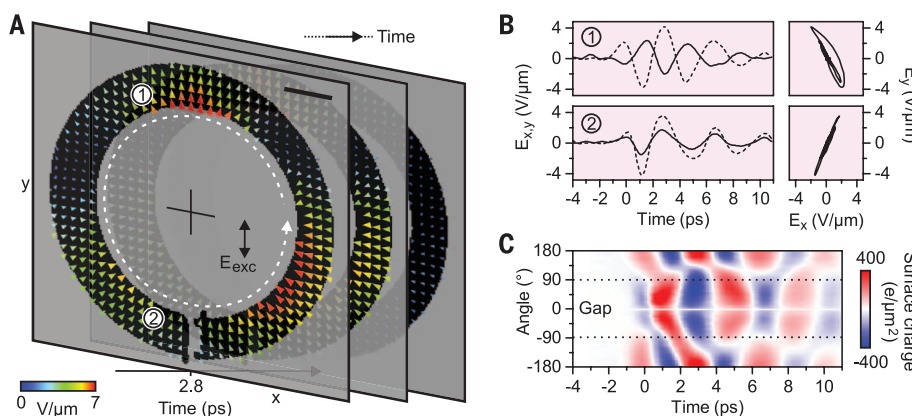


Fig. 3. Space-time-field results in a split-ring resonator. (A) Time-frozen electric field vectors at three delay times (full results in movie S3). Scale bar, 100 μm . (B) Time-dependent fields (left) and polarizations (right) at locations (1) and (2) in (A). (C) Space-time map of the surface carrier density at the inner edge [(A), white dashed line].

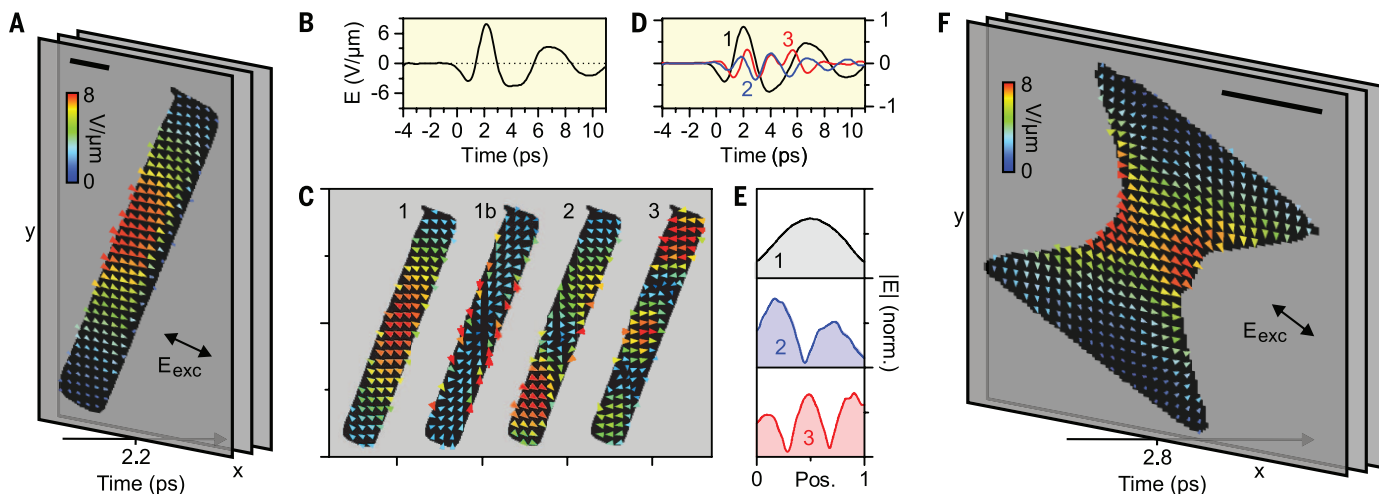


Fig. 4. Rectangle and butterfly resonators. (A) Time-frozen electric field vectors at 2.2 ps delay (full results in movie S4). (B) Time-dependent field at the center. (C) First four modes revealed through singular value decomposition. (D) Time traces (amplitudes, scaled) of modes 1, 2, and 3. (E) Electric field strengths along a line through the center. (F) Butterfly resonator, electric field vectors at 2.8 ps delay (full results in movie S5). Scale bars, 100 μm .

Fig. 4A (full results in movie S4). The waveform in the center is shown in Fig. 4B. The frequency at early times is higher than at later times, when the oscillations show a nonharmonic shape with damped peak regions. This indicates the presence of multiple modes at different frequencies, but phase-locked. In order to find those, we invoked a principle component analysis via singular value decomposition. The first four modes are depicted in Fig. 4C; further ones have no clear shape or time structure anymore. Three of the modes have a series of maxima that are almost equidistantly distributed over the slit length. Mode 1b is different and has a shape with vortex polarization; we attribute this to residual magnetic field effects (17) and a slight tilt of the structure with respect to the electron beam. The time traces from the decomposition matrix are shown in Fig. 4D. Mode 1 is centered at 0.20 THz, mode 2 at 0.39 THz, and mode 3 at 0.54 THz. Cuts through the modes along the slit's long axis at center are shown in Fig. 4E. Evident are one, two, and three spatial maxima, respectively, but with some asymmetries and slightly elliptical polarization in modes 2 and 3. Singular value decomposition neither assumes any electromagnetic boundary conditions nor enforces harmonic-oscillator solutions. That nevertheless a series of oscillation orders with dispersion and nontrivial phase relations can be identified is a virtue of the complete spatial, temporal, and vectorial data set obtained with waveform electron microscopy. In the butterfly-shaped resonator (Fig. 4F and movie S5), there is only one mode excited (frequency, 0.3 THz; damping, ~ 5 ps). The field enhancement at 2.8 ps is ~ 9 close to the metal and ~ 6 in the middle, which is lower than desirable, because the rounded crests of our structure apparently disperse the field lines at the center.

The ability to record field vectors in space and time is essentially a consequence of the electron's charge, which is usually detrimental in ultrafast microscopy via space charge effects, but here the

charge is exploited as a local, sensitive, directional, and noninvasive probe of electromagnetic field cycles. We estimate the angular and spatial resolutions achievable in a state-of-the-art instrument at few-nanometer resolution by invoking a ray-optical analysis (17). The result is plotted in fig. S4 in dependence on defocus. Letting the spatial resolution degrade by only a factor of two from the optimum value is already sufficient for an angular resolution below 20 μrad . Via Eq. 1 and assuming a 100-nm-deep structure along the z axis, we obtained a measurable field strength of ~ 0.0026 V/nm or ~ 1 V per 40 nm, which overlaps with the conditions in working electronic or plasmonic circuitry. In the experiment, the angular resolution was 60 to 80 μrad (17), which is close to $\alpha_{\text{em}} \approx 60$ μrad of the beam. At reasonable signal-to-noise levels, the illumination's uncorrelated divergence determines the angular resolution. The ultimate limit with coherent femtosecond emitters (27) and a wave-based analysis (6, 7) is defined by the de Broglie wavelength of the electrons.

Magnetic fields, which are important in negative-index metamaterials or memory devices, can be revealed and separated from the electric-field deflections by making two experiments at different electron velocities; the electric parts of the Lorentz force scales proportionally to $1/v_e^2$, whereas the magnetic deflection follows a $1/v_e$ law. Energy-filtered imaging can measure forward momentum changes and, in combination with tomography, reveal the complete electric and magnetic vector fields in space and time. Surface studies with a scanning electron microscope are also feasible, given its sensitivity to (transient) surface voltages, energy losses, or secondary electron trajectory asymmetries.

Microwave-compressed (18), photon-gated (21), or deflection-selected (20) electron pulses are approaching the few-femtosecond regime of pulse duration. This allows waveform imaging at multi-terahertz frequencies, faster than any electronic

devices available. Metamaterials operate at light-wave frequencies, at which ~ 1 -fs resolution is required for subcycle sampling. Recently, attosecond electron pulse trains (28) have been realized in an electron microscope (29). With cycle-synchronous excitation and probing (28), waveform electron microscopy will enable a direct visualization of nanophotonic phenomena at lightwave frequencies. Isolated attosecond electron pulses may potentially be generated via single-electron wavepacket compression (18) or ponderomotive effects (22) and will be useful for studying nonlinear or strong-field phenomena that are not reversible between adjacent excitation cycles.

In principle, any light-matter interaction starts with atomic-scale charge displacements, and waveform electron microscopy at subatomic resolution (5, 6) could potentially reveal those motions. More straightforward, however, will be studies of collective carrier dynamics and field effects in nanoscale devices—for example, in electronics, metamaterials, nanophotonic circuitry, near-field sensors, or light-harvesting nanostructures. That waveform imaging and shape characterization now require only one instrument—the electron microscope—will likely be advantageous for such investigations.

REFERENCES AND NOTES

1. P. E. Batson, N. Dellby, O. L. Krivanek, *Nature* **418**, 617–620 (2002).
2. R. Erni, M. D. Rossell, C. Kisielowski, U. Dahmen, *Phys. Rev. Lett.* **102**, 096101 (2009).
3. A. H. Zewail, *Science* **328**, 187–193 (2010).
4. R. J. D. Miller, *Science* **343**, 1108–1116 (2014).
5. N. Shibata *et al.*, *Nat. Phys.* **8**, 611–615 (2012).
6. K. Müller *et al.*, *Nat. Commun.* **5**, 5653 (2014).
7. M. J. Humphry, B. Kraus, A. C. Hurst, A. M. Maiden, J. M. Rodenburg, *Nat. Commun.* **3**, 730 (2012).
8. B. Barwick, D. J. Flannigan, A. H. Zewail, *Nature* **462**, 902–906 (2009).
9. J. Cummings, A. Zettl, M. R. McCartney, J. C. H. Spence, *Phys. Rev. Lett.* **88**, 056804 (2002).
10. M. Lohr *et al.*, *Ultramicroscopy* **117**, 7–14 (2012).
11. N. Shibata *et al.*, *Sci. Rep.* **5**, 10040 (2015).

12. M. Müller, A. Paarmann, R. Ernstorfer, *Nat. Commun.* **5**, 5292 (2014).
13. E. Najafi, T. D. Scarborough, J. Tang, A. Zewail, *Science* **347**, 164–167 (2015).
14. A. Yurtsever, R. M. van der Veen, A. H. Zewail, *Science* **335**, 59–64 (2012).
15. E. Quinonez, J. Handali, B. Barwick, *Rev. Sci. Instrum.* **84**, 103710 (2013).
16. L. Piazza *et al.*, *Nat. Commun.* **6**, 6407 (2015).
17. Materials and methods are available as supplementary materials on Science Online.
18. A. Gliserin, M. Walbran, F. Krausz, P. Baum, *Nat. Commun.* **6**, 8723 (2015).
19. C. Kealhofer *et al.*, *Science* **352**, 429–433 (2016).
20. A. Lassisse, P. H. A. Mutsaers, O. J. Luiten, *Rev. Sci. Instrum.* **83**, 043705 (2012).
21. M. T. Hassan, H. Liu, J. S. Baskin, A. H. Zewail, *Proc. Natl. Acad. Sci. U.S.A.* **112**, 12944–12949 (2015).
22. L. J. Wong, B. Freelon, T. Rohwer, N. Gedik, S. G. Johnson, *New J. Phys.* **17**, 013051 (2015).
23. N. I. Zheludev, *Science* **328**, 582–583 (2010).
24. A. V. Kildishev, A. Boltasseva, V. M. Shalae, *Science* **339**, 1232009 (2013).
25. R. A. Shelby, D. R. Smith, S. Schultz, *Science* **292**, 77–79 (2001).
26. X. Ni, Z. J. Wong, M. Mrejen, Y. Wang, X. Zhang, *Science* **349**, 1310–1314 (2015).
27. D. Ehberger *et al.*, *Phys. Rev. Lett.* **114**, 227601 (2015).
28. P. Baum, A. H. Zewail, *Proc. Natl. Acad. Sci. U.S.A.* **104**, 18409–18414 (2007).
29. A. Feist *et al.*, *Nature* **521**, 200–203 (2015).

ACKNOWLEDGMENTS

This work was supported by ERC and Munich-Centre for Advanced Photonics. We thank F. Krausz for awesome support and discussions and acknowledge I. Zhuraviev (Vocord SoftLab) for help with GPU programming.

SUPPLEMENTARY MATERIALS

www.sciencemag.org/content/353/6297/374/suppl/DC1
Materials and Methods
Figs. S1 to S4
References (30–36)
Movies S1 to S5

13 April 2016; accepted 23 June 2016
10.1126/science.aaf8589

WATER RESOURCES

Connections between groundwater flow and transpiration partitioning

Reed M. Maxwell^{1*} and Laura E. Condon²

Understanding freshwater fluxes at continental scales will help us better predict hydrologic response and manage our terrestrial water resources. The partitioning of evapotranspiration into bare soil evaporation and plant transpiration remains a key uncertainty in the terrestrial water balance. We used integrated hydrologic simulations that couple vegetation and land-energy processes with surface and subsurface hydrology to study transpiration partitioning at the continental scale. Both latent heat flux and partitioning are connected to water table depth, and including lateral groundwater flow in the model increases transpiration partitioning from 47 ± 13 to $62 \pm 12\%$. This suggests that lateral groundwater flow, which is generally simplified or excluded in Earth system models, may provide a missing link for reconciling observations and global models of terrestrial water fluxes.

Evapotranspiration (ET) is the largest terrestrial water flux, typically accounting for more water than runoff and for about 60% of precipitation (I). It contributes a substantial portion of the global land-energy budget (2) as latent heat (LH) flux, which affects regional climate (3). Evapotranspiration commonly refers to the combination of all evaporation (E) from bare soil, water bodies, plant canopy, and sublimation from snow, and transpiration (T) through plant stoma during photosynthesis. Here we focus on the partitioning of ET into bare soil E and plant T . Because T depends on plant processes, whereas E depends on shallow soil moisture and energy availability, these two factors respond differently to physical drivers and stress. Disentangling these fluxes over large scales is a key step toward improved understanding and prediction of watershed dynamics, especially when considering future stresses.

Connectivity between the surface and the subsurface provides a fundamental control on water-energy fluxes and partitioning (4). Connections

between the water table and evapotranspiration have been shown in model simulations (5 – 9) and observations of regional systems (10). Although theory to estimate and simulate evapotranspiration has evolved much over past decades (11), lateral groundwater flow has yet to be incorporated in continental-scale partitioning estimates (12). Quantifying the role of groundwater is important, because if partitioning is tied to water table depth and lateral flow, accurate predictions of future water availability will require a more detailed understanding of the underlying processes controlling groundwater surface water interactions than are currently included in most Earth system simulators. Current research on partitioning relies on either isotope approaches or land surface models (13). These are fundamentally different methods, but both make critical assumptions about groundwater contributions to T and simplify groundwater surface water interactions. Discrepancies in partitioning estimates remain, and some have suggested that it may be systematically underestimated by current Earth system models (13 , 14).

We used a continental-scale integrated hydrology model simulation to study the role that lateral groundwater flow plays in evapotranspiration partitioning (15). We used the ParFlow model (16 , 17), which couples groundwater and surface water flow with vegetation processes and snow dynamics (7 , 18) to solve a complete water and

energy balance [figs. S1, S2, and S4 (15)]. The domain covers 6.3 million km^2 and encompasses major river basins in North America [including the Mississippi, Colorado, and Ohio basins; see Fig. 1 and fig. S3 (15)]. Simulations were run for one water year at hourly resolution driven by reconstructed meteorology. Transient simulations were initialized using the results of a prior steady-state model over the same domain (19) and additional transient model initialization [tables S1 and S2 (15)]. The model was compared to 1.2 million transient observations of stream flow, groundwater, and snow, and was shown to match observed behavior [figs. S5 to S20 (15)].

This simulation generated roughly 1.3 trillion outputs over the 1-year period, covering all key components of the water energy budget. Two variables that exemplify hydrologic stores and land-energy fluxes—water table depth and LH flux (the energy counterpart to ET)—show many scales of detail within these output fields (Fig. 1). For example, although groundwater is generally shallower in the more humid eastern region of the domain and deeper in arid western regions, laterally convergent flow drives local variability, creating shallow water tables in river valleys that can supply surface water export. We see similar patterns in LH flux, large-scale trends also driven by climate gradients, yet nested hillslope-scale fluctuations persist.

The integrated model we used provides the ability to explicitly evaluate interactions between variables that are excluded from other global approaches (i.e., water table depth and individual land-energy flux components such as T and E). For example, the ratios of plant transpiration to total evapotranspiration (T/ET) are calculated directly from model outputs and compared to compiled stand-scale (14) and global (4 , 20 , 21) isotopically based partitioning estimates [Fig. 2, A and B (15)]. We see broad agreement between model simulations and estimates across scale; the domain-averaged T/ET of $62 \pm 12\%$ agrees with recent global isotopically derived estimates (4 , 14 , 20 , 21).

To determine the role of lateral groundwater flow in these partitioning estimates, we performed a second simulation that is identical to the base case but allowed only vertical water movement, with no topographic influences or lateral flow. This approach is similar to current practice in land surface models (15). This “no lateral flow” simulation resulted in a domain-averaged T/ET

¹Integrated GroundWater Modeling Center, Department of Geology and Geological Engineering, Colorado School of Mines, Golden, CO, USA. ²Department of Civil and Environmental Engineering, Syracuse University, Syracuse, NY, USA.

*Corresponding author. Email: rmxwell@mines.edu